**Zhe Gao**
Department of Industrial and Systems Engineering, Rutgers, The State University of New Jersey, Piscataway, NJ 08854
e-mail: zg96@scarletmail.rutgers.edu

**Haris Ali Khan**
Department of Industrial and Manufacturing Engineering, The Pennsylvania State University, University Park, PA 16802;
Aerospace Engineering Department, College of Aeronautical Engineering, National University of Sciences and Technology, H-12, Islamabad 44000, Pakistan
e-mail: hakhan@cae.nust.edu.pk

**Jingjing Li**
Mem. ASME
Department of Industrial and Manufacturing Engineering, The Pennsylvania State University, University Park, PA 16802
e-mail: jul572@psu.edu

**Weihong (Grace) Guo**[1]
Mem. ASME
Department of Industrial and Systems Engineering, Rutgers, The State University of New Jersey, Piscataway, NJ 08854
e-mail: wg152@soe.rutgers.edu

# Sensor Fusion and On-Line Monitoring of Friction Stir Blind Riveting for Lightweight Materials Manufacturing

*This research focused on developing a hybrid quality monitoring model through combining the data-driven and key engineering parameters to predict the friction stir blind riveting (FSBR) joint quality. The hybrid model was formulated through utilizing the in situ processing and joint property data. The in situ data involved sensor fusion (force and torque signals) and key processing parameters (spindle speed, feed rate, and stacking sequence) for data-driven modeling. The quality of the FSBR joints was defined by the tensile strength. Furthermore, the joint cross-sectional analysis and failure modes in lap shear tests were employed to confirm the efficacy of the proposed model and development of the process–structure–property relationship.* [DOI: 10.1115/1.4052907]

*Keywords: online monitoring, sensor fusion, tensor decomposition, feature extraction, quality inspection, lightweight materials manufacturing, welding and joining*

## 1 Introduction

Carbon fiber-reinforced polymer (CFRP) composites are lightweight materials that have been increasingly used in many industries for their relatively high strength-to-weight ratio compared to other materials [1–3]. One of the notable applications of CFRP composites is in the automotive industry for lightweighting, where CFRP composites are joined with different metals to obtain dissimilar materials structure. On a broader spectrum, the joining techniques for CFRP with dissimilar materials can be divided into two categories. The first category can be classified as welding where different techniques such as ultrasonic welding [4], friction stir welding [5], and laser welding [6] have been mostly used. The second category is mechanical fastening [7], where a rivet, screw, bolt, or stud is usually utilized to mechanically join two or more pieces together. Friction stir blind riveting (FSBR) is a promising one-sided joining technique that integrates the advantages of both friction stirring welding and mechanical riveting [8]. During the last decade, FSBR has demonstrated its superiority in manufacturing sound dissimilar materials joints where different metals such as Al, Fe, and Mg have been successfully joined [9,10]. In addition, researchers have also employed FSBR for joining CFRP with metals such as Al and Mg [11]. However, most of the existing studies about FSBR process optimization relied on utilizing the ex situ results from destructive testing (i.e., the maximum load from tensile tests) and tensile failure modes to determine the process window [12,13]. Furthermore, the available studies analyzed single-point data, i.e., maximum penetration force and maximum torque, retrospectively, while the rich information hidden in the real-time force and torque signals was not extracted or explored [14]. To ensure robust control of the FSBR process, therefore, it demands an online quality monitoring methodology that can capture the variations in the process. This study addresses this challenge with five approaches: (1) by representing the FSBR force and torque signals in tensor objects and introducing tensor decomposition methods to extract features from the signals, whereas the two signals were handled separately previously; (2) by considering the general case of FSBR with various process parameters, whereas one specific experimental setting is employed previously; (3) by extending the feature selection method to handle continuous and categorical features simultaneously, while only continuous features were considered in Ref. [15]; (4) by optimizing a weighted classifier fusion method to estimate the quality of FSBR joints, whereas arbitrarily chosen classifiers for quality evaluation were used earlier; and (5) by developing a process–structure–property (PSP) linkage through correlating process parameters, mechanical property (maximum load), and joint structure.

This research, therefore, focuses on developing a sensor fusion and online process monitoring method to enable quality evaluation of the FSBR process. This goal was realized by analyzing the real-time data of state variables, i.e., penetration force and torque signals recorded during the FSBR joining of CFRP and aluminum alloy 6111 (AA6111) sheets. For this purpose, machine learning protocols were applied to establish the relationship between the process variables and the quality of the joints (maximum load) by integrating feature extraction, feature selection, and classifier fusion. In this research, features extracted from the in situ signals were combined with critical parameters defined based on

[1]Corresponding author.

Manuscript received August 24, 2021; final manuscript received October 25, 2021; published online December 3, 2021. Assoc. Editor: Jaydeep Karandikar.

engineering knowledge to provide quality evaluations for the joints. Furthermore, cross-sectional analysis was performed and related to the predicted quality to evaluate the model performance. A PSP linkage was hence established by integrating the quality (property), joint cross sections (structure), and state variables (process).

## 2 Materials and Experimental Procedure

Aluminum alloy sheets (AA5754-O) and injection molded CFRP (Polyamide 66 matrix with 40 wt% carbon fiber with a fiber length of 300–500 $\mu$m) each with a thickness of 3 mm were utilized for manufacturing FSBR joints. Table 1 presents the mechanical properties of the two workpiece materials. SSPV-86 Monobolt, blind rivet, was used in this research where the shoulder diameter was 6.5 mm, tip diameter was 6.4 mm, and the length under the rivet head was 23.7 mm. The rivet was made of medium carbon steel with a hollow mandrel tip and zinc coating. The shear and tensile strength of the rivet were 10,675 N and 8,229 N, respectively [13].

In this study, the FSBR process is utilized to fabricate lap sheer joints from two material stack-up combinations, AA6111-CFRP (AA6111 is the top sheet) and CFRP-AA6111 (CFRP is the top sheet), at various spindle speeds ($\omega = 3000$ and 5000 rpm) and feed rates ( $v = 120$ and 420 mm/min). Furthermore, a dynamometer for recording the force and torque signals was fastened with the fixture. Details of the FSBR process can be found in Ref. [12] while the experimental setup is provided in Fig. 1.

Quasi-static tensile testing was performed to classify the joint quality using an Instron 5500R universal testing machine under a constant displacement rate of 3 mm/min at room temperature. Table 2 provides the number of joints manufactured using a specific experimental setting and the number in parentheses represents the number of joints subject to tensile test, for instance 49 CFRP-AA6111 FSBR joints were obtained using a feed rate of 120 mm/min and 5000 rpm where eight joints were subjected to tensile test. Not all joints were tested due to time and cost constraints.

A Nikon microscope was used for acquiring cross-sectional images of the FSBR joint where the metallurgical sample was first mounted in epoxy and then cross sectioned using a precision diamond saw blade. The samples were then polished with silicon papers following a sequence of #320, #600, and #800, and finally polished with diamond suspensions down to 1 $\mu$m.

## 3 Data Filtering and Selection Technique

**3.1 Force and Torque Signals.** During the process, the penetration force and torque data were recorded at discrete time intervals, i.e., after every 0.01 s. Figure 2(*a*) shows the raw signals in fabricating an AA6111-CFRP joint under $\omega = 3000$ rpm and $v = 120$ mm/min. It is noted that the raw dataset contains a lot of irrelevant data points recorded before and after the actual FSBR process. To remove the irrelevant data points in the raw signals, the start and end times of each process were identified and then the data were extracted for 6 s (Total time for the process is 6 s. Start time was defined when there is an increase in the force signals and end time is defined when there was an abrupt increase at the end of the process due to the constant force applied from the machine

**Table 1 Mechanical properties of the constituent materials [13]**

| Materials | Young's modulus (GPa) | Yield strength (MPa) | Tensile strength (MPa) | Elongation (%) |
|---|---|---|---|---|
| AA5754-O (Al) | 70 | 102 | 234 | 21 |
| CFRP (PA66 with 40% carbon fiber) | 20.68 | No data | 248.2 | 1–3 |

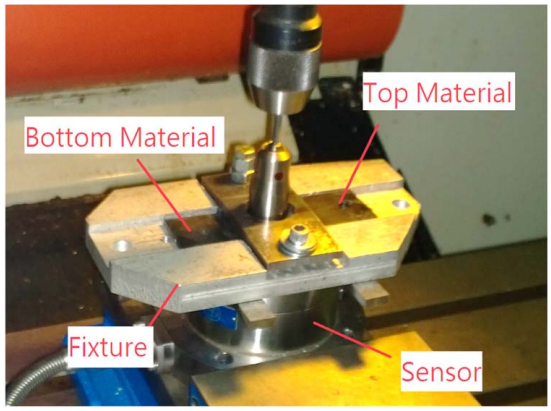


**Fig. 1 FSBR process setup, adapted from Ref. [12]**

**Table 2 Number of FSBR samples**

| Feed rate, $v$ (mm/min) | Spindle speed, $\omega$ (rpm) | Number of samples (number with tensile test) | |
|---|---|---|---|
| | | AA6111-CFRP | CFRP-AA6111 |
| 120 | 3000 | 4 (1) | 3 (1) |
| | 5000 | 4 (3) | 49 (8) |
| 420 | 3000 | 3 (0) | 3 (2) |
| | 5000 | 4 (0) | 4 (3) |

spindle after the rotation stops). Furthermore, to remove noises from the multi-sensor nonlinear profile data, the data profiles were represented in high-dimensional arrays and tensor decomposition methods were used to extract features from the original multi-sensor data. For this purpose, the wavelet method was utilized to localize the patterns in the signal which provides the advantage of preserving the important signal features while removing noise. Figure 2 is an example of the collected penetration force and torque data during the process, where Fig. 2(*b*) shows the de-noised and truncated signals for the raw signals in Fig. 2(*a*). It can be seen that wavelets can effectively de-noise the force and torque signals while preserving their original complex shapes.

After pre-processing, the force and torque signals are represented in a three-way array $\mathcal{A}$, which is a tensor object $\mathcal{A} \in \mathbb{R}^{600\times2\times N}$, where 600 is the number of data points collected on each signal, two is the number of sensors, and $N = 74$ is the number of samples. Figure 2(*b*) shows that the pre-processed signals are nonlinear with complex shapes and possible sensor-to-sensor correlation. The scatter plot of the pre-processed force and torque signals is shown in Fig. 3. It can be observed that many data points in Fig. 3 are in the vicinity of the diagonal line, indicating a strong correlation between the two signals.

The correlation coefficient was further calculated between the pre-processed force and torque signals for all the $N = 74$ joints. The boxplot of the correlation coefficients is given in Fig. 4. The correlation coefficients range from 0.0608 to 0.9058, with average 0.6952, median 0.7419, first quartile 0.6058, and third quartile 0.8194. Hence, there is a significant correlation between the force and torque signals in FSBR experiments, which should not be ignored. Therefore, tensor decomposition methods that can analyze the two signals together are needed to extract features from $\mathcal{A}$.

**3.2 Tensile Testing Data.** The maximum tensile loads of the joints were extracted and used as the quality response of those joints. Figure 5(*a*) presents the maximum tensile load data for the considered configurations where the first number in experiment

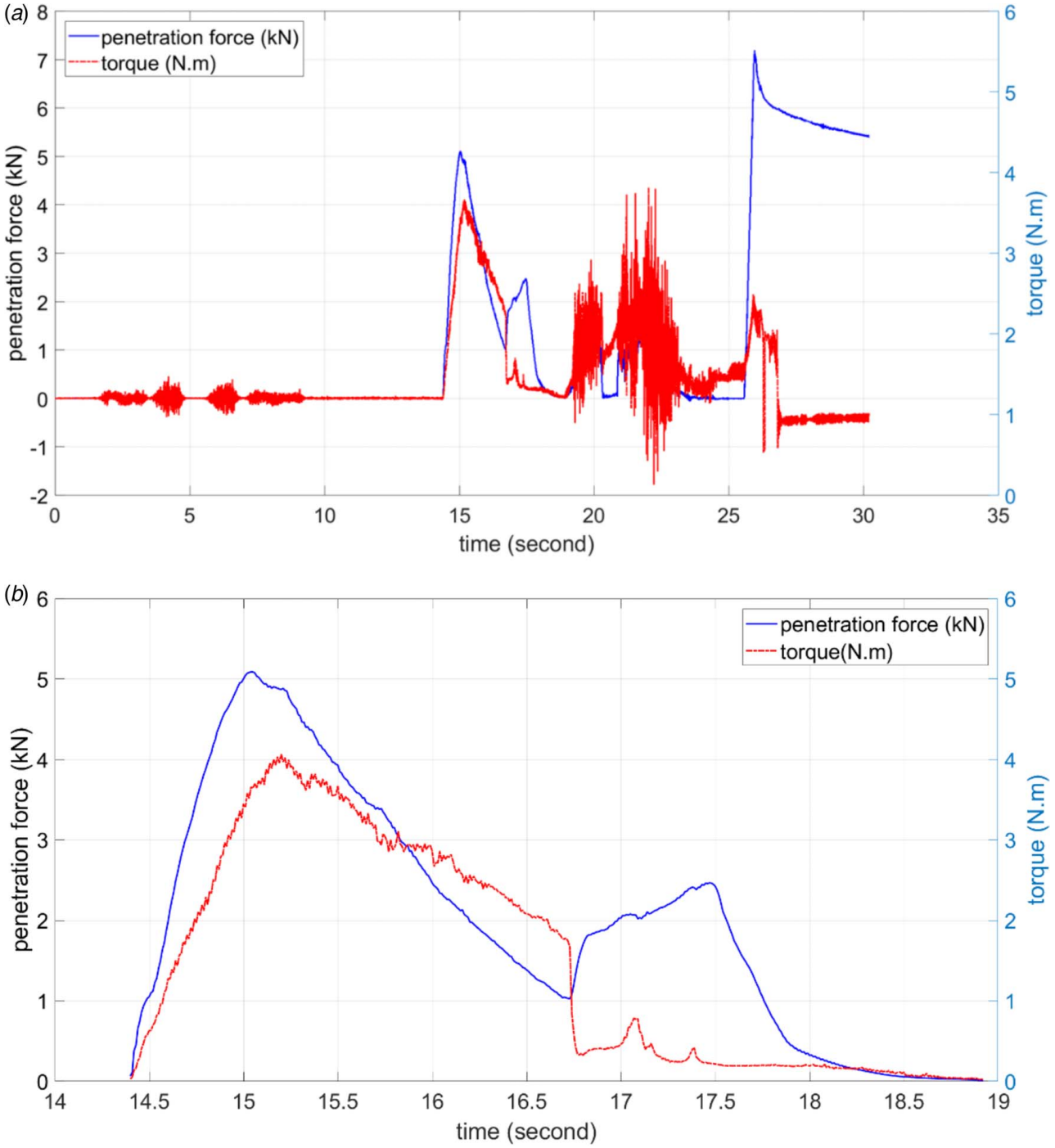


**Fig. 2 Force and torque signals of an AA6111-CFRP joint under $\omega = 3000$ rpm and $v = 120$ mm/min: (*a*) raw signals and (*b*) pre-processed signals**

setting represents rpm, second number represents feed rate, and the alphabets represent stacking sequence. For example, 3000-120 AC represents 3000 rpm, 120 mm/min, and aluminum as the top sheet. The tested joints were then clustered into two quality groups based on their maximum tensile loads where Fig. 5(*b*) presents the dendrogram of hierarchical clustering.

Two quality groups were obtained, namely, the low-quality group, denoted by $\Omega_0 = \{i: L_i < L_0, i = 1, \ldots, N_1\}$, and high-quality group, denoted by $\Omega_1 = \{i: L_i > L_0, i = 1, \ldots, N_1\}$, where $L_i$ is the maximum tensile load of sample $i$ and $L_0$ is the decision boundary. Based on the quality groups, we assign the quality response of sample $i$ to be $y_i = 0$ if $i \in \Omega_0$ and $y_i = 1$ if $i \in \Omega_1$. As shown in Fig. 5(*b*), among the $N_1 = 18$ joints that had tensile tests, eight samples are in the low-quality group, $\Omega_0 = \{2, 3, 4, 5, 10, 11, 12, 13\}$, and 10 samples are in the high-quality group, $\Omega_1 = \{1, 6, 7, 8, 9, 14, 15, 16, 17, 18\}$.

## 4 Methodology

**4.1 Overview.** The key steps in the proposed method for FSBR process monitoring and quality evaluation are shown in

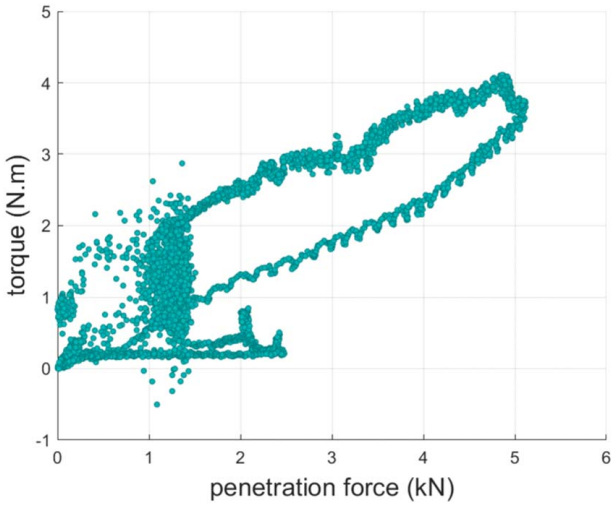


**Fig. 3 Scatter plot of force and torque signals from Fig. 2(*b*)**

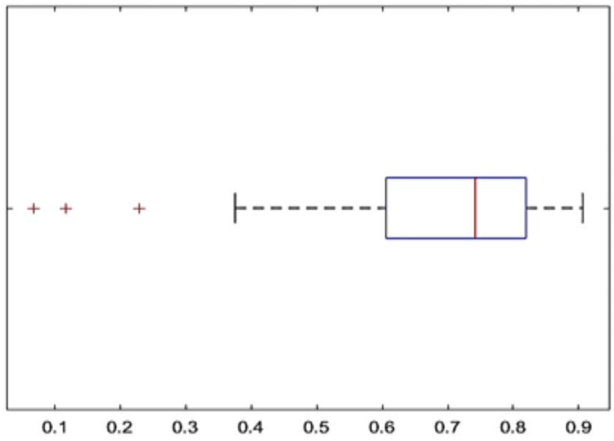

**Fig. 4 Boxplot of the correlation coefficients between the pre-processed force and torque signals**

Fig. 6. Information about the FSBR process includes parameters in the experiment setup, material stack-up sequence, and the recorded force and torque signals. In step 1, engineering-driven features are extracted from the signals. Two lower rank tensor decomposition (LRTD) algorithms, multilinear principal component analysis (MPCA) [16], and uncorrelated multilinear principal component analysis (UMPCA) [17] are introduced to extract features from the three-way array, $\mathcal{A}$, representation of the signals, based on multilinear tensor-to-vector or tensor-to-tensor projections. Details of the algorithms can be found in Refs. [16,17]. In step 2, the sparse group lasso (SGL) regression method is applied to select the most significant features from the extracted features. Selected features are then fed into five individual classifiers in step 3. The results from individual classifiers are fused with optimal weights to obtain the final classification results that indicate the predicted quality of FSBR joints. Quality information of the FSBR joints is needed in step 2 and step 3 so that the best features can be selected and that the classifiers can be optimized. The details of each step will be elaborated in the following subsections.

By integrating feature extraction, feature selection, and classifier fusion, the proposed method establishes the relationship between the FSBR process and joint quality. The proposed method is then applied to the samples which were not subjected to mechanical testing (tensile test) so that their quality can be estimated. The proposed method will also provide online monitoring of the FSBR process.

**4.2 Feature Extraction.** It is critical to effectively extract features from the raw signals to provide useful information about the FSBR process. Experimental settings—feed rate, spindle speed, and material stack-up sequence—are represented as categorical features. Each feature has two levels, as listed in Table 3. Section 4.2.1 will elaborate on the details on extracting engineering-driven features based on our understanding of the process. Section 4.2.2 will introduce the LRTD algorithms for extracting data-driven features.

*4.2.1 Extracting Engineering-Driven Features.* Existing studies on FSBR have identified a few important features based on the physical understanding of the process, such as the maximum force value during the penetration of the top sheet, maximum torque value, the energy consumed, and the time duration of the process [11,18]. Taking these findings as well as expert knowledge into consideration, a total of 12 engineering-driven features are defined. They are illustrated in Fig. 7 and described in Table 4.

During the penetration of the top workpiece in FSBR, the maximum force $F_1$ is recorded at the time $t_1$, at which time the torque is $M_1$. At time $t_v$, the rivet penetrates through the top workpiece and touches the interface between the top and bottom workpieces; the force at the time $t_v$ is $F_v$ and the torque is $M_v$. The rivet then continues to penetrate the bottom workpiece and the maximum force $F_2$ is recorded at the time $t_2$ with torque $M_2$. In addition, the maximum torque during FSBR is denoted as $M_{\max}$. The duration of the entire FSBR process is $T$ and the duration of the

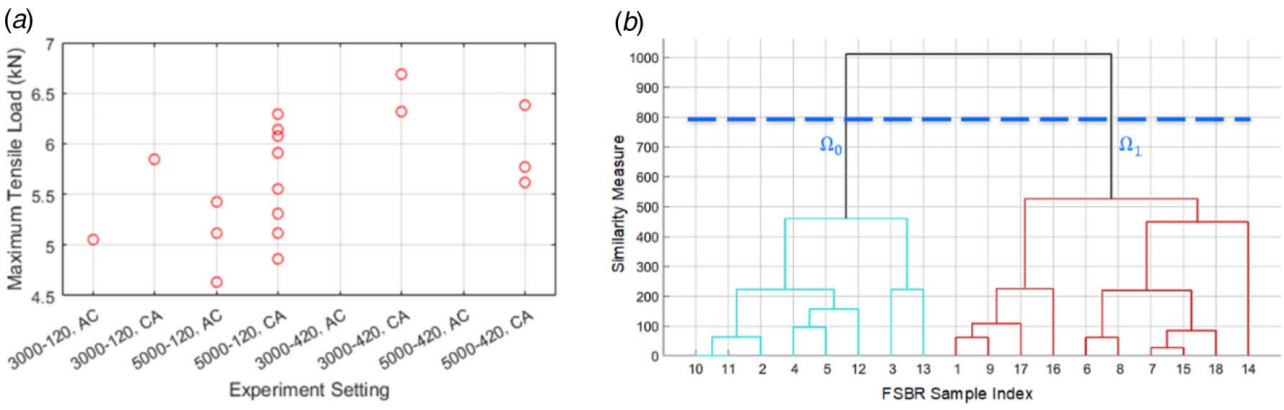


**Fig. 5 (*a*) Maximum tensile loads of AA6111-CFRP (AC) and CFRP-AA6111 (CA) joints at various spindle speeds and feed rates and (*b*) clustering result of the FSBR samples: low-quality group $\Omega_0 = \{2, 3, 4, 5, 10, 11, 12, 13\}$ and high-quality group $\Omega_1 = \{1, 6, 7, 8, 9, 14, 15, 16, 17, 18\}$**

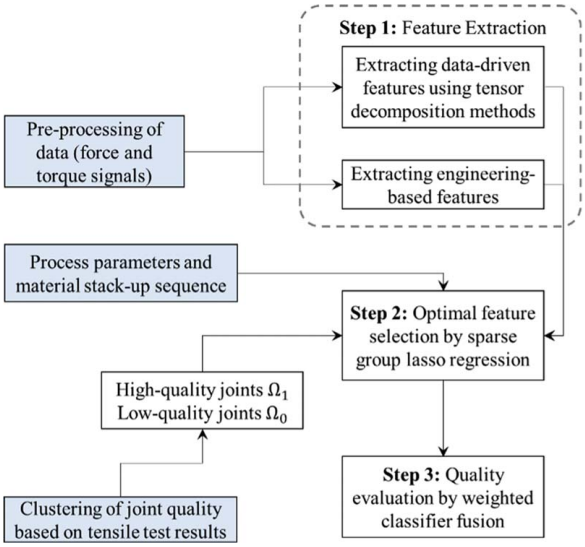


**Fig. 6 Flowchart of the proposed method**

**Table 3 Summary of categorical features**

| Feature | Description |
|---|---|
| AC/CA | AA6111-CFRP (AA6111 is the top sheet) or CFRP-AA6111 (CFRP is the top sheet) |
| Feed rate | $v = 120$ or 420 mm/min |
| Spindle speed | $\omega = 3000$ or 5000 rpm |

penetration of the top sheet is $T_1$. Features $S_1$ and $S_2$ represent the energy consumed by the force during the penetration of the top sheet and bottom sheet, respectively. Similarly, feature $E$ represents the energy consumed by the torque during FSBR. The energy features are calculated as the area under the force or torque curve. All these features are continuous.

*4.2.2 Extracting Data-Driven Features.* Although engineering-driven features can effectively represent certain characteristics of the process, a lot of important information is still hidden in the complex shapes of the signals and the sensor-to-sensor correlations. Therefore, unsupervised feature extraction methods are needed to effectively reduce the dimensionality of the original signals and to extract data-driven features that contain important information about the FSBR process.

The principal component analysis (PCA) is a well-understood method and used the unsupervised multivariate technique to explain the variance–covariance structure through a few linear combinations of the original variables [19,20]. Multilinear extensions of the PCA allow applying the PCA technique to tensors without unfolding the original dataset.

Two tensor decomposition algorithms, MPCA [16] and UMPCA [17], for multi-sensor data, are used in this research. The tensor representation of the FSBR force and torque signals is $\mathcal{A} \in \mathbb{R}^{L \times J \times N}$, where $L = 600$ is the number of data points collected on each signal, $J = 2$ is the number of sensors, and $N$ is the number of samples.

**4.3 Optimal Feature Selection.** The FSBR process is adequately represented by the extracted features, which include categorical features that represent the experimental settings, 12 continuous features from the force and torque signals based on engineering knowledge, and $(P_1P_2 + 1)$ continuous features from MPCA or $P_0 \leq 2$ continuous features from UMPCA. Let $\mathcal{F}$ denote the set of extracted features and $P = |\mathcal{F}|$ is the total number of extracted features.

Although a total of $N = 74$ joints was fabricated, only the $N_1 = 18$ joints that had tensile tests can be used to train the quality evaluation model. Since $N_1$ (number of tested joints) is not large compared to $P$ (total number of extracted features), feature selection is needed to identify the most significant features. Feature selection allows the simplification of the quality evaluation model so that it is easier to interpret. A good selection of features also enables shorter model training times, helps to avoid the curse of dimensionality (especially if $P_1P_2$ is relatively large), and enhances model generalization by reducing overfitting [21,22].

Since both continuous and categorical features are present in the extracted features, the feature selection method in this study should effectively handle mixed-type data. Therefore, the SGL regression method is adopted as a feature selection method in this study. Categorical features are treated as grouped features in SGL. Each continuous feature is treated as a group of size one. For feature selection, SGL is superior to group lasso in the sense that SGL selects features with the consideration of groupwise and within-group sparsity [23–25].

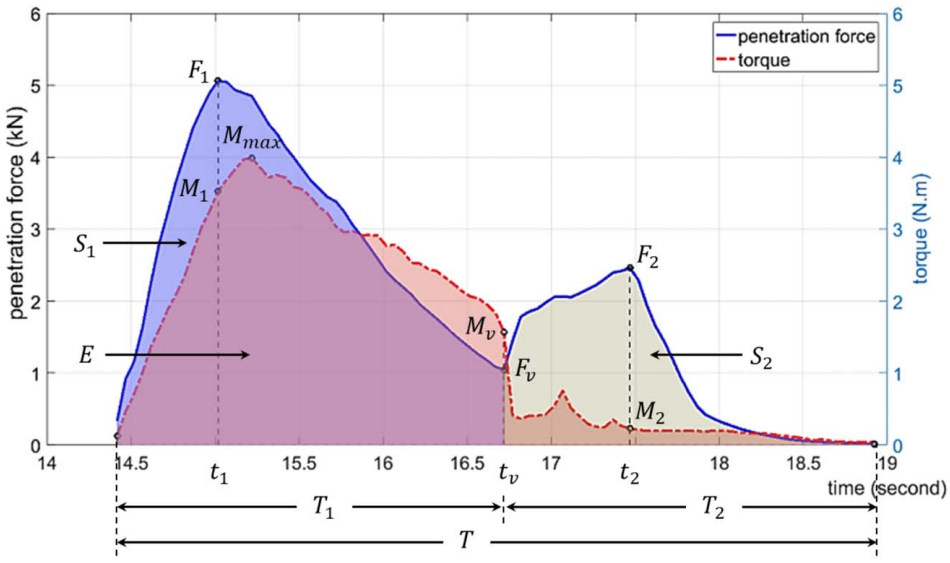


**Fig. 7 Engineering-driven features from Fig. 2's AA6111-CFRP joint**

**Table 4 Summary of engineering-driven features**

| Feature | Description |
|---|---|
| $F_1$ | Maximum force value during the penetration of the top sheet |
| $F_2$ | Maximum force value during the penetration of the bottom sheet |
| $F_v$ | Valley force value during the penetration towards the bottom sheet |
| $M_1$ | Torque value when $F_1$ is recorded |
| $M_2$ | Torque value when $F_2$ is recorded |
| $M_v$ | Torque value when $F_v$ is recorded |
| $M_{\max}$ | Maximum torque value during the FSBR process |
| $T_1$ | The time duration of the penetration of the top sheet |
| $T$ | The time duration of the entire FSBR process |
| $S_1$ | The area under the force signal in $T_1$ |
| $S_2$ | The area under the force signal in $T_2 = T - T_1$ |
| $E$ | The area under the torque signal in $T$ |

Let $\boldsymbol{X}$ denote the $N$ by $P$ matrix of extracted features for all samples and $\boldsymbol{X}_1 \in \mathbb{R}^{N_1 \times P}$ denote the matrix of extracted features for the $N_1$ samples with a quality response. Let $\boldsymbol{y}$ denote the response vector of length $N_1$. The SGL regression extends lasso (Least Absolute Shrinkage and Selection Operator) regression by introducing two penalty terms to the objective function:

$$\hat{\boldsymbol{\beta}}_{\text{SGL}} = \underset{\boldsymbol{\beta}}{\operatorname{argmin}} \frac{1}{2N_1} \|\boldsymbol{y} - \sum_{k=1}^{K} \boldsymbol{X}_1^{(k)} \boldsymbol{\beta}^{(k)}\|_2^2 + (1-\alpha)\lambda \sum_{k=1}^{K} \|\boldsymbol{\beta}^{(k)}\|_2 + \alpha\lambda \|\boldsymbol{\beta}\|_1 \quad (1)$$

where $K$ is the number of feature groups, and $\boldsymbol{X}_1^{(k)}$ is the submatrix of $\boldsymbol{X}_1$ with columns corresponding to the predictors in the $k$th feature group, $k = 1, \ldots, K$. The $k$th group has $J_k$ features and thus $\boldsymbol{X}_1^{(k)} \in \mathbb{R}^{N_1 \times J_k}$. Vector $\boldsymbol{\beta}^{(k)} \in \mathbb{R}^{J_k \times 1}$ is the coefficient vector of the $k$th group. $\boldsymbol{\beta} = \{\boldsymbol{\beta}^{(k)}\}_k$ represents the regression coefficients for all groups.

In Eq. (1), $\|\boldsymbol{y} - \sum_{k=1}^{K} \boldsymbol{X}_1^{(k)} \boldsymbol{\beta}^{(k)}\|_2^2$ is the sum of squared errors for the grouped features; $\sum_{k=1}^{K} \|\boldsymbol{\beta}^{(k)}\|_2$ is the $l_2$ norm to account for the number of groups selected; $\|\boldsymbol{\beta}\|_1$ is the $l_1$ norm to account for the number of individual features selected. The two penalty terms are controlled by the groupwise sparsity parameter $\alpha$ and within-group sparsity parameter $\lambda$, respectively. If $\alpha = 1$, Eq. (1) reduces to lasso regression; if $\alpha = 0$, SGL reduces to group lasso regression. The SGL model can be fitted via an accelerated generalized gradient algorithm with backtracking [26–28].

In this study, features are selected based on the available knowledge of $\boldsymbol{X}_1$ and $\boldsymbol{y}$. The optimal values for $\alpha$ and $\lambda$ are determined by leave-one-out cross-validation. The selected features are represented in the set $\tilde{\mathcal{F}} \subseteq \mathcal{F}$ with $\tilde{P} = |\tilde{\mathcal{F}}| \leq P$. $\tilde{\boldsymbol{X}}_1 \in \mathbb{R}^{N_1 \times \tilde{P}}$ is the matrix of selected features for the $N_1$ samples with quality responses. Applying $\tilde{\mathcal{F}}$ to $\boldsymbol{X}$, we obtain $\tilde{\boldsymbol{X}} \in \mathbb{R}^{N \times \tilde{P}}$ as the matrix of selected features for all the $N$ samples; let $\tilde{\boldsymbol{X}}_2 \in \mathbb{R}^{N_2 \times \tilde{P}}$ denote the matrix of selected features for the $N_2$ samples without quality response.

**4.4 Quality Evaluation.** A weighted classifier fusion method is developed to establish the relationship between the selected features and the quality response of the FSBR joints. Multiple classifiers are employed to overcome the large bias or large variance associated with the implementation of an individual classifier. The proposed fusion approach classifier weights the probability outputs of individual classifiers and then sums them up to estimate a final probability, based on which the class label is assigned. The proposed approach is different from the traditional weighted majority voting approach, the outputs of individual classifiers are weighted and linearly summed up, and the class label with the largest weight is chosen as the final classifier fusion result [29].

Since quality evaluation for FSBR is essentially a binary classification problem, the probability of assigning sample $i$ to the high-quality group $\Omega_1$ will be estimated in each classifier. Let $\pi_i^c$ denote the probability that classifier $c$ assigns sample $i$ to $\Omega_1$. The probabilities $\pi_i^c$ will be weighted and fused to obtain the final probability estimation. The proposed fusion approach is different from the traditional weighted majority voting approach since it relies more on the probability outputs rather than the class labels. The rationale behind the proposed approach is elaborated in the following intuitive example. If sample $i$ has $\pi_i^1 = 0.95$ with class label 1 and $\pi_i^2 = 0.45$ with class label 0, assuming equal weights for the two classifiers, the traditional voting approach would produce a tie between label 0 and label 1, whereas the proposed approach would give a final probability of $\pi_i = (\pi_i^1 + \pi_i^2)/2 = 0.7$, which indicates that class label 1 should be assigned to sample $i$. The result from the proposed fusion approach is consistent with our intuition since $\pi_i^1$ is close to 1, indicating high confidence in the classification, while $\pi_i^2$ is close to 0.5, indicating uncertainty in the classification.

In the proposed weighted classifier fusion approach, $\tilde{\boldsymbol{X}}_1$, the matrix of selected features for the $N_1$ samples with the quality response and the quality response $\boldsymbol{y}$ are fed into five individual classifiers to obtain the probability outputs, which are then fused to obtain the FSBR quality evaluation model.

*4.4.1 Individual Classifiers.* The individual classifiers adopted in the proposed fusion approach are logistic regression, kernel support vector machine (KSVM) with the polynomial kernel, KSVM with Gaussian kernel, neural network, and $k$-nearest neighbors. These five classifiers are chosen to address different types of patterns in the dataset.

*4.4.2 Weighted Classifier Fusion.* The estimated probability that classifier $c$ assigns sample $i$ to $\Omega_1$ is denoted as $\hat{\pi}_i^c$. The probabilities from individual classifiers are weighted and linearly summed up to obtain the fused probability estimation as shown in Eq. (2):

$$\hat{\pi}_i = \sum_{c=1}^{C} w_c \times \hat{\pi}_i^c \quad (2)$$

where $w_c$ is the weight for the $c$th classifier; $\sum_{c=1}^{C} w_c = 1$ and $0 \leq w_c \leq 1$, $c = 1, \ldots, C$. $\hat{\pi}_i$ is the final estimated probability that sample $i$ is assigned to $\Omega_1$. The class label is then assigned by comparing $\hat{\pi}_i$ to a threshold $\pi_0$, represented in a logistic function as follows:

$$\hat{y}_i = \frac{1}{1 + e^{-a(\hat{\pi}_i - \pi_0)}} \quad (3)$$

where $\hat{y}_i$ is the predicted class label for sample $i$; $a$ is the convergence rate so that $\hat{y}_i = 1$ if $\hat{\pi}_i \geq \pi_0$ and $\hat{y}_i = 0$ if $\hat{\pi}_i < \pi_0$.

The performance of the weighted classifier fusion approach is evaluated by the correct classification rate (CCR). If all the $N_1$ samples are considered in this evaluation, then the CCR

**Table 5 Selected features by SGL**

| Tensor decomposition method<br>SGL parameters | MPCA | UMPCA |
|---|---|---|
| $(\alpha^*,\ \lambda^*)$ | $\tilde{\mathcal{F}}_A = \{F_1, \text{PC}_1, \text{PC}_3, \text{AC/CA}\}$ | $\tilde{\mathcal{F}}_B = \{F_1, \text{PC}_1, \text{AC/CA}\}$ |
| $(\alpha = 0.95,\ \lambda^*)$ | $\tilde{\mathcal{F}}_C = \{F_1, \text{PC}_1, \text{PC}_3, \text{AC/CA}, v, \omega\}$ | $\tilde{\mathcal{F}}_D = \{F_1, \text{PC}_1, \text{AC/CA}, v, \omega\}$ |

is estimated by

$$\widehat{\mathrm{CCR}} = 1 - \frac{|\hat{\boldsymbol{y}} - \boldsymbol{y}|^0}{N_1} \tag{4}$$

where $\hat{\boldsymbol{y}}$ denotes the estimated class label vector of length $N_1$, calculated by Eq. (3); $\boldsymbol{y}$ is the true response vector as obtained by quality definition in Sec. 2. $|\hat{\boldsymbol{y}} - \boldsymbol{y}|^0$ is the $l_0$ "norm" that counts the number of non-zero entries of the vector $\hat{\boldsymbol{y}} - \boldsymbol{y}$.

In the proposed fusion approach, the weights $w_c$ should be optimized so that the CCR can be maximized. Optimal weights are therefore obtained by cross-validation. In $k$-fold cross-validation, as each of the $k$ subsamples are used as the validation data, a CCR result is obtained. The $k$ CCR results from the folds can then be averaged to produce an average CCR, denoted as $\overline{\mathrm{CCR}}$. The standard deviation of the $k$ CCR results is $s_{\mathrm{CCR}}$. Therefore, the optimal weights maximize $\overline{\mathrm{CCR}}$ while keeping $s_{\mathrm{CCR}}$ small. Furthermore, the definition of signal-to-noise ratio (SNR) is employed to obtain the optimal weights by

$$\boldsymbol{w}^* = \arg \max_{\boldsymbol{w}} \ \mathrm{SNR} = \arg \max_{\boldsymbol{w}} \ \overline{\mathrm{CCR}}/s_{\mathrm{CCR}} \tag{5}$$

where $\boldsymbol{w}$ is the vector of $w_c$'s.

Once the parameters, including the optimal weights, in the classifier fusion approach, are obtained, the quality evaluation model can be expressed as

$$\hat{y}_i = \frac{1}{1 + e^{-a\left(\sum_{c=1}^{C} w_c^* \times \hat{\pi}_i^c - \pi_0\right)}} \tag{6}$$

FSBR joint $i$ is classified into the low-quality group $\Omega_0$ if $\hat{y}_i = 0$; we assign $i \in \Omega_1$, the high-quality group, if $\hat{y}_i = 1$.

## 5 Results

Data-driven features are extracted from tensor $\mathcal{A} \in \mathbb{R}^{600\times2\times74}$ of the FSBR force and torque signals by MPCA and UMPCA. In MPCA, by keeping $\theta = 80\%$ of the total variation, $\mathcal{A}$ is projected onto a low-dimensional tensor $\mathcal{S} \in \mathbb{R}^{3\times1\times74}$. The $L = 600$ data points collected on each signal are projected onto $P_1 = 3$ features; the $J = 2$ sensors are projected onto $P_2 = 1$ feature. The residual tensor $\mathcal{E}$ then represents 20% of the total variation. A total of $(P_1P_2 + 1) = 4$ features are extracted by MPCA. In UMPCA, since the number of extracted features is limited by 2, $P_0 = 2$ uncorrelated features were extracted from $\mathcal{A}$. The data-driven features from either MPCA or UMPCA are then combined with the 12 engineering-driven features and three experimental setting parameters to form the feature set $\mathcal{F}$. $P = |\mathcal{F}| = 15 + (P_1P_2 + 1) = 19$ if MPCA is adopted and $P = 15 + P_0 = 17$ if UMCPA is adopted.

**5.1 Feature Selection.** In feature selection, categorical features are treated as grouped features in SGL. The feed rate and spindle speed are combined into a feature group of size four that represents the process parameters. "AC/CA" is treated as a group of size two that represents the material stack-up sequence. Each continuous feature is treated as a group of size one. Table 5 shows the results of optimal feature selection by SGL.

The optimal sparsity parameters are $(\alpha^*, \lambda^*)$, determined by leave-one-out cross-validation. When data-driven features from MPCA are adopted, the selected features are $\{F_1, \mathrm{PC}_1, \mathrm{PC}_3, \mathrm{AC/CA}\}$, denoted by a set $\tilde{\mathcal{F}}_A$, where $\mathrm{PC}_1$ and $\mathrm{PC}_3$ represent the first and third principal components extracted from MPCA. When data-driven features from UMPCA are adopted, the selected features are $\{F_1, \mathrm{PC}_1, \mathrm{AC/CA}\}$, denoted by a set $\tilde{\mathcal{F}}_B$, where $\mathrm{PC}_1$ represents the first principal component extracted from UMPCA. As listed in Table 3, $F_1$ is the engineering-driven feature that represents the maximum force during the penetration of the top sheet in FSBR.

Two critical process parameters—feed rate $v$ and spindle speed $\omega$—are not selected by the $(\alpha^*, \lambda^*)$ SGL. To include these features in the selected set, $\alpha$ is fixed to 0.95 and $\lambda^*$ is then determined by leave-one-out cross-validation. When features from MPCA are adopted, the selected features are $\{F_1, \mathrm{PC}_1, \mathrm{PC}_3, \mathrm{AC/CA}, v, \omega\}$, denoted by the set $\tilde{\mathcal{F}}_C$; when features from UMPCA are adopted, the selected features are $\{F_1, \mathrm{PC}_1, \mathrm{AC/CA}, v, \omega\}$, denoted by a set $\tilde{\mathcal{F}}_D$. These four scenarios are denoted as $A$, $B$, $C$, and $D$.

Following the notations in Sec. 4.2, we let $\tilde{\boldsymbol{X}}_A \in \mathbb{R}^{N\times\tilde{P}_A}$ denote the matrix of selected features of the set $\tilde{\mathcal{F}}_A$ for all the $N$ samples, $\tilde{P}_A = |\tilde{\mathcal{F}}_A|$. $\tilde{\boldsymbol{X}}_A$ is further split into $\tilde{\boldsymbol{X}}_{1A} \in \mathbb{R}^{N_1\times\tilde{P}_A}$ and $\tilde{\boldsymbol{X}}_{2A} \in \mathbb{R}^{N_2\times\tilde{P}_A}$ for the samples with and without quality responses, respectively. Similarly, for the selected feature subsets $\tilde{\mathcal{F}}_B$, $\tilde{\mathcal{F}}_C$, and $\tilde{\mathcal{F}}_D$, we obtain matrices $\tilde{\boldsymbol{X}}_B \in \mathbb{R}^{N\times\tilde{P}_B}$, $\tilde{\boldsymbol{X}}_C \in \mathbb{R}^{N\times\tilde{P}_C}$, and $\tilde{\boldsymbol{X}}_D \in \mathbb{R}^{N\times\tilde{P}_D}$. Each matrix is further split into two matrices: $\tilde{\boldsymbol{X}}_{1B} \in \mathbb{R}^{N_1\times\tilde{P}_B}$, $\tilde{\boldsymbol{X}}_{1C} \in \mathbb{R}^{N_1\times\tilde{P}_C}$, and $\tilde{\boldsymbol{X}}_{1D} \in \mathbb{R}^{N_1\times\tilde{P}_D}$ for the $N_1$ samples with the quality response; $\tilde{\boldsymbol{X}}_{2B} \in \mathbb{R}^{N_2\times\tilde{P}_B}$, $\tilde{\boldsymbol{X}}_{2C} \in \mathbb{R}^{N_2\times\tilde{P}_C}$, and $\tilde{\boldsymbol{X}}_{2D} \in \mathbb{R}^{N_2\times\tilde{P}_D}$ for those without a quality response.

**Table 6 Optimal weights for weighted classifier fusion**

| Scenario | Optimal weights Dataset | $w_{\mathrm{lr}}^*$ | $w_{\mathrm{psvm}}^*$ | $w_{\mathrm{gsvm}}^*$ | $w_{\mathrm{nn}}^*$ | $w_{\mathrm{knn}}^*$ |
|---|---|---|---|---|---|---|
| $A$ | $\tilde{\boldsymbol{X}}_A$ | 0.0516 | 0.0214 | 0.0347 | 0.3929 | 0.4995 |
| $B$ | $\tilde{\boldsymbol{X}}_B$ | 0.0000 | 0.0293 | 0.0273 | 0.4377 | 0.5057 |
| $C$ | $\tilde{\boldsymbol{X}}_C$ | 0.1824 | 0.1354 | 0.0345 | 0.6477 | 0.0000 |
| $D$ | $\tilde{\boldsymbol{X}}_D$ | 0.2970 | 0.2764 | 0.2037 | 0.2228 | 0.0000 |

**5.2 Weighted Classifier Fusion.** The individual classifiers in the proposed fusion approach are (i) logistic regression, (ii) KSVM with polynomial kernel of degree $d = 2$, (iii) KSVM with the Gaussian kernel of $\gamma = 0.25$ and non-separable penalty parameter of 100, (iv) neural network with a single hidden layer, eight nodes in the hidden layer, and a decay rate of $\eta = 0.1$ to help reduce overfitting, and (v) $k$-nearest neighbors with $k = 7$. The fusion model in Eq. (6) has $\pi_0 = 0.5$ as the decision boundary and $a = 1000$ as the convergence rate.

Cross-validation is used to determine the optimal weights in classifier fusion. Taking all $N_1$ samples into consideration, the optimal weights for each feature subset are shown in Table 6. $w_{\mathrm{lr}}^*$, $w_{\mathrm{psvm}}^*$, $w_{\mathrm{gsvm}}^*$, $w_{\mathrm{nn}}^*$, and $w_{\mathrm{knn}}^*$ are the optimal weights for logistic regression, polynomial KSVM, Gaussian KSVM, neural network, and $k$-nearest neighbors, respectively.

The $N_1 = 18$ samples with quality responses are divided into a training dataset and a testing dataset by stratified sampling. Specifically, the testing dataset contains four samples: two randomly selected from the low-quality group $\Omega_0$ and two from the high-quality group $\Omega_1$. Since $\Omega_0$ contains eight samples and $\Omega_1$ contains ten samples, the total number of unique datasets is

$$\binom{8}{2} \times \binom{10}{2} = 1260$$

The proposed method is applied to each unique partition to obtain a training CCR and a testing CCR. Considering all 1260 unique partitions, $\overline{\mathrm{CCR}}$, $s_{\mathrm{CCR}}$, and $\mathrm{SNR} = \overline{\mathrm{CCR}}/s_{\mathrm{CCR}}$ values were obtained and the results are shown in Table 7.

The following observations are deduced from Table 7. All scenarios have high $\overline{\mathrm{CCR}}$ and small $s_{\mathrm{CCR}}$ for the training dataset. The highest training $\overline{\mathrm{CCR}}$ is obtained in scenario D while the smallest training $s_{\mathrm{CCR}}$ is obtained in scenario C (the obtained values are marked in italics). Scenario C yields the highest training SNR. Scenarios B and D also give high SNR results for the training dataset (the obtained values are marked in italics). Scenario B yields the best result for the testing dataset by looking at the combined values with respect to the highest $\overline{\mathrm{CCR}}$ and smallest $s_{\mathrm{CCR}}$. It is therefore inferred that the feature subset in scenario B gives the best quality classification results.

**Table 7 Quality classification results**

| Scenario | SGL parameters | Tensor decomposition method | Training performance | | | Testing performance | | |
|---|---|---|---|---|---|---|---|---|
| | | | $\overline{\text{CCR}}$ | $s_{\text{CCR}}$ | SNR | $\overline{\text{CCR}}$ | $s_{\text{CCR}}$ | SNR |
| *A* | $(\alpha^*,\ \lambda^*)$ | MPCA | 0.8791 | 0.0469 | 18.7346 | 0.8011 | 0.1729 | 4.6338 |
| *B* | $(\alpha^*,\ \lambda^*)$ | UMPCA | 0.8916 | 0.0402 | *22.1740* | *0.8584* | *0.1499* | *5.7251* |
| *C* | $(\alpha = 0.95,\ \lambda^*)$ | MPCA | 0.9468 | *0.0325* | *29.0977* | 0.7849 | 0.1704 | 4.6056 |
| *D* | $(\alpha = 0.95,\ \lambda^*)$ | UMPCA | *0.9513* | 0.0429 | *22.1964* | 0.7278 | 0.1849 | 3.9355 |

For the online monitoring of FSBR, it is recommended to first extract features by UMPCA, then selecting the optimal feature subset $\tilde{\mathcal{F}}_B = \{F_1, \text{PC}_1, \text{AC/CA}\}$, and finally determining the quality of the FSBR joints by weighted classifier fusion with optimal weights $\boldsymbol{w}^* = (0.0000, 0.0293, 0.0273, 0.4377, 0.5057)^T$. Based on these results, the quality evaluation model in Eq. (7) can be rewritten as

$$\hat{y}_i = \frac{1}{1 + \exp\left(-1000 \times [(\boldsymbol{w}^* \times h_c(\tilde{\boldsymbol{X}}_{B,i})) - 0.5]\right)} \tag{7}$$

where $h_c$ represents the $c$th individual classifier, $c = 1, \ldots, 5$. $\tilde{\boldsymbol{X}}_{B,i}$ is the $i$th row in the matrix $\tilde{\boldsymbol{X}}_B$, representing the $i$th sample in FSBR joints. $\hat{y}_i$ is the prediction label for the $i$th sample. $\hat{y}_i = 0$ indicates that the $i$th sample is classified into the low-quality group $\Omega_0$, whereas $\hat{y}_i = 1$ indicates that the $i$th sample is classified into the high-quality group $\Omega_1$.

The developed model is then applied to the FSBR samples that do not have a quality response. Among the $N_2 = 56$ joints that were not tested, 48 are predicted as of high quality and eight samples are predicted as of low quality.

**5.3 Comparison With Traditional Methods.** In this subsection, the importance of extracting data-driven features from the force and torque signals together via tensor decomposition is demonstrated. Comparison in the performance of the proposed method with two "traditional" methods is drawn, where in M1 only engineering-driven features are considered; in M2, data-driven features are also considered but these features are extracted from the two signals separately. The comparison results are summarized in Table 8.

In M1, the 12 extracted engineering-driven features (see Table 3) are fed into weighted classifier fusion. The optimal weights for the five individual classifiers are determined as {0.4000, 0.1737, 0.1481, 0.2345, 0.0437}. The quality evaluation results in both training and testing datasets are shown in Table 8. It can be observed from Table 8 that the performance of M1 suffers from severe overfitting. In an attempt to reduce overfitting, feature selection via LASSO is performed, which yielded only one significant feature out of the 12 engineering-driven features. The selected feature is $T_1$, the time duration to penetrate the top layer. Expert knowledge on FSBR, along with the preliminary analysis, suggests that $T_1$ alone cannot fully represent the complex FSBR process. Hence, all the 12 engineering-driven features in M1 are selected.

In M2, the two signals are treated separately, ignoring possible correlation, as opposed to analyzing them together in the proposed method. Applying PCA to the force signals resulted in four PCs when keeping 95% variance of the original data; applying PCA to the torque signals resulted in seven PCs when keeping 95% variance of the original data. With 11 PCs and 12 engineering-driven features, feature selection via LASSO is performed, which yielded seven significant features, $\{F_1,\ M_1,\ M_v,\ S_1,\ \text{PC}F_1,\ \text{PC}T_1,\ \text{PC}T_4\}$, including four engineering-driven features ($F_1$, $M_1$, $M_v$, $S_1$ as described in Table 3) and three data-driven features, where $\text{PC}F_1$ is the first PC from the force signals, and $\text{PC}T_1$ and $\text{PC}T_4$ represent the first and the fourth PCs from the torque signals. The seven selected features are then fed into weighted classifier fusion. The optimal weights for the five individual classifiers are determined as {0.3000, 0.1746, 0.1609, 0.2660, 0.0986}. The quality evaluation results are also shown in Table 8. It is noticed that M2 outperformed M1, indicating the importance of adding data-driven features. The engineering-driven features, although carefully defined, are not able to fully represent the complex FSBR process, providing inferior results in quality evaluation.

Table 8 also shows that the proposed method in scenario B outperforms M2. Recall that scenario B has three selected features for quality evaluation while M2 has seven. When using tensor decomposition, the proposed method can achieve more accurate results with fewer features, facilitating fast and early quality inspection. The superiority of the proposed method can be explained from two aspects: (1) the force and torque signals are analyzed together since high correlation exists between the two signals; this sensor-to-sensor correlation can be effectively handled by the multilinear extensions of PCA; (2) the proposed method incorporates process settings and material stack-up sequence with the extracted features, providing more information about the FSBR process; this addition is enabled by representing them as categorical features and adopting SGL to handle mixed-type data. Both aspects contribute to the superiority of the proposed method.

**5.4 Process–Structure Relationship.** A total of four joint configurations were selected from the $N_2$ dataset (whose quality is not experimentally tested) for cross-sectional analysis to validate the performance of the quality model. Among them, two configurations are selected from predicted low-quality joints and the remaining two are selected from predicted low-quality joints. Furthermore, for the predicted high-quality joints, each sample is picked from scenario C and scenario D (defined in Sec. 5.2), respectively.

**Table 8 Comparing quality evaluation results with traditional methods**

| Traditional method | Training performance | | | Testing performance | | |
|---|---|---|---|---|---|---|
| | $\overline{\text{CCR}}$ | $s_{\text{CCR}}$ | SNR | $\overline{\text{CCR}}$ | $s_{\text{CCR}}$ | SNR |
| M1 | 1.0000 | 0.0000 | N/A | 0.4608 | 0.2264 | 2.0346 |
| M2 | 1.0000 | 0.0000 | N/A | 0.7545 | 0.1856 | 4.0648 |
| Proposed method, scenario B (from Table 7) | 0.8916 | 0.0402 | *22.1740* | *0.8584* | *0.1499* | *5.7251* |

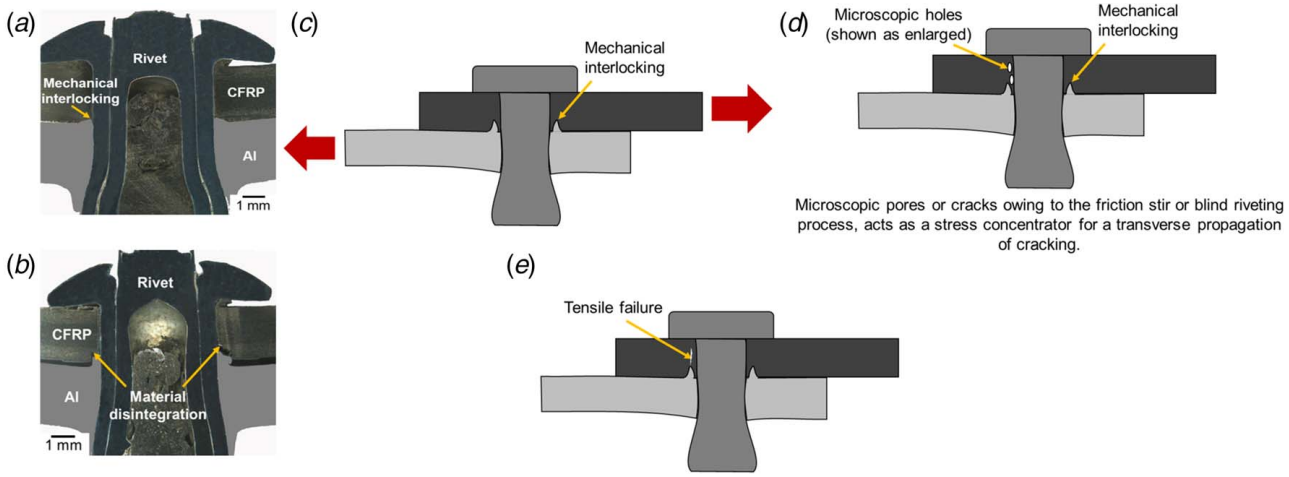


**Fig. 8 (*a*) and (*b*) Cross sections of joints with mechanical interlocking, and (c), (*d*), and (e) schematic illustration of tensile failure mode: (c) joint lap shear testing of the joint, (*d*) microscopic pores or cracks owing to the friction stirring or blind riveting process, acts as a stress concentrator for a transverse propagation of cracking, and (e) final tensile failure perpendicular to the direction of loading**

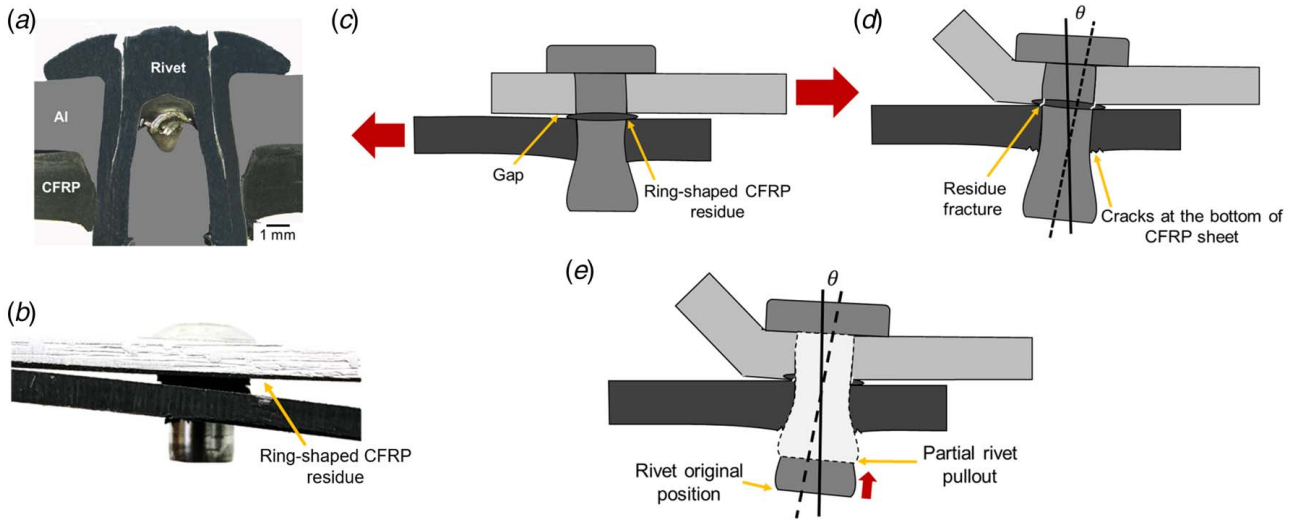


**Fig. 9 (*a*) Cross section of joint without mechanical interlocking, (*b*) front view of the joint with thick ring-shaped CFRP residue and no mechanical interlocking, (c), (*d*), and (e) schematic of partial rivet pullout failure mode in AC configuration: (c) lap shear testing of the joint (thick horizontal arrows indicate the direction of loading), (*d*) cracks appearing at the bottom of CFRP sheet and residue fracture along with nonregular secondary bending of Al sheet, and (e) partial rivet pull out failure mode, where the thick upward arrow indicates the upward motion of the rivet and different rivet colors (dark or light) are indicative of rivet initial and final position after the pullout**

Figures 8(*a*) and 8(*b*) present cross sections of predicted high-quality joints. The joint shown in Fig. 8(*a*) is chosen from scenario D (UMPCA method) and manufactured with 5000 rpm spindle speed, 120 mm/min feed rate, and the CFRP sheet is placed on the top, i.e., CA stacking sequence. The joint presented in Fig. 8(*b*) is chosen from scenario C (MPCA method) and manufactured with 5000 rpm spindle speed, 420 mm/min feed rate, and the CFRP sheet is placed on the top, i.e., CA stacking sequence. Both Figs. 8(*a*) and 8(*b*) revealed no gap between the rivet and the worksheet. However, material disintegration at the bottom of CFRP sheet is observed in Fig. 8(*b*). Moreover, mechanical interlocking as described in Ref. [11] is evident in Figs. 8(*a*) and 8(*b*) (CA stacking sequence). In previous research [11], the authors suggested that the mechanical interlocking served as a key contributor in the final failure mode of the joint as it prevents rivet slippage and (or) shearing. For the two cases in consideration, the tested joints of the similar configuration revealed tensile failure (Figs. 8(*c*)–8(*e*)). With regard to the proposed model, scenario D gives the best result for the testing dataset by looking at the combined values with respect to the highest $\overline{\text{CCR}}$ and small $s_{\text{CCR}}$.

From the process mechanics perspective, material disintegration is owed to insufficient heat generation which is attributable to two phenomena. The first contributing phenomenon is the lower friction coefficient between CFRP and steel, i.e., 0.3 [30], compared to the friction coefficient between Al and steel, i.e., 0.6.[1] Low friction coefficient value between the rivet and workpiece material results in a prolonged sliding-dominant contact condition [31], which tends to prolonged drilling conditions and higher material removal rate [32]. The second attributable phenomenon is a high feed rate which inhibits sufficient material softening. Consequently, some material gets detached from CFRP when the Al material tried to form the interlock. Moreover, material disintegration occurred at the bottom of the CFRP sheet and results in random force signals

[1]https://www.engineersedge.com/coeffients_of_friction.htm

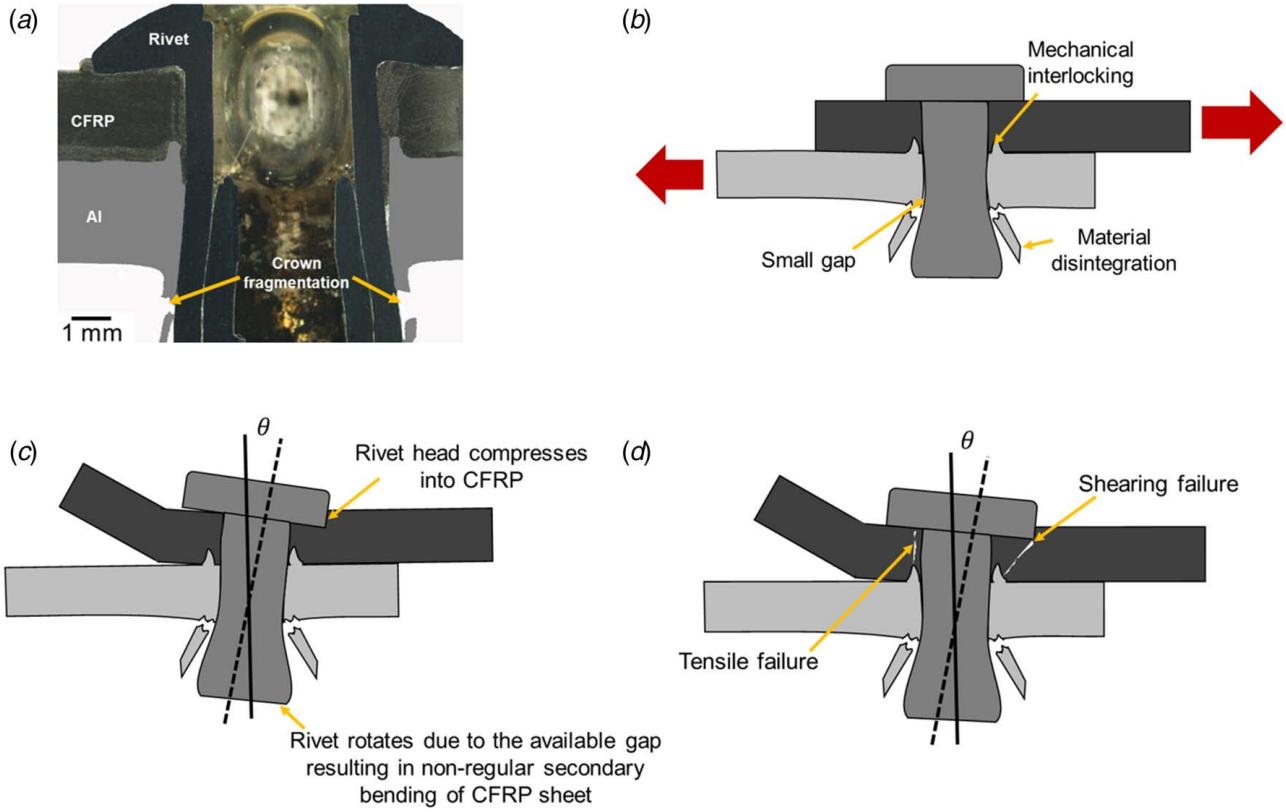


**Fig. 10 (*a*) Cross section of joint with crown fragmentation, (*b*), (c), and (*d*) schematic of mixed failure mode in CA configuration: (*b*) small gaps occur at the material disintegrated region of the Al sheet upon loading (thick horizontal arrows indicate the direction of loading), (c) rivet head compresses into the CFRP sheet due to rivet rotation along with nonregular secondary bending in CFRP sheet, and (*d*) mixed failure (tensile + shear) mode**

(noise) which can be confirmed through higher SNR value. Therefore, scenario D utilizing UMPCA method provides better quality prediction than scenario C (MPCA method) which is also predicted through data analysis (Sec. 5.2).

The cross sections of the predicted low-quality joints are presented in Figs. 9(*a*) and 10(*a*). The joint configuration shown in Fig. 9(*a*) is manufactured using 5000 rpm spindle speed, 120 mm/min feed rate, and the Al sheet is placed on the top, i.e., AC stacking sequence. Rate is devoid of mechanical interlocking (Fig. 9(*a*)). Figure 10(*a*) shows the joint cross section with 3000 rpm spindle speed, 420 mm/min feed rate, and CA stacking sequence. Both the configurations are selected from scenario D as it was previously confirmed as the optimized scenario. Two different failure modes, i.e., partial rivet pullout and mixed failure (shear + tensile failure), were observed.

For the joint without mechanical interlocking (Fig. 9(*a*)), partial rivet pullout failure mode occurs rather than tensile failure mode (Figs. 8(*c*)–8(*e*)). In scenarios where the CFRP sheet is placed at the bottom, in addition to the absence of mechanical interlocking, a ring-shaped residue is formed at the surface of the CFRP sheet as the molten material is unable to penetrate the top Al worksheet (Fig. 9(*b*)). The ring-shaped residue results in the gap between the two sheets. During the lap shear testing, small cracks are generated at the bottom of the CFRP sheet which results in loosening of contact between the rivet and CFRP sheet (Fig. 9(*c*)). Further application of the load allows the rivet to rotate and move up (Fig. 9(*d*)). Simultaneously, change in the loading conditions causes secondary bending of the Al sheet, thereby preventing complete rivet pullout (Fig. 9(*e*)). Visual inspection of the other FSBR joints with AC stacking sequence revealed that the ring-shaped residue becomes thinner when a low feed rate and high spindle speed are being utilized because of the generation of more work. Moreover, the gap between the two sheets increases with the increasing thickness of ring-shaped residue and resulted in the low-quality joint in some cases, particularly where a high feed rate and low spindle speed are employed.

Crown fragmentation is evident at the bottom of the Al sheet in Fig. 10(*a*). Low spindle speed (3000 rpm) and high feed rate (420 mm/min) result in insufficient heat generation to soften the material. When the rivet tip reached the bottom surface of the workpiece, the material deforms resulting in crown formation [18]. For the considered case, crown fragmentation occurs due to a high penetration force. It is explained that upon lap shear testing, the bond between the Al rivet and Al sheet got disintegrated from the bottom of the worksheet resulting in a small gap (Fig. 10(*b*)). The gap continues to grow further as the test progresses thereby allowing the rivet to rotate in the generated gap. The rotation of the rivet changes the loading conditions, thereby introducing the nonregular secondary bending [11] in the CFRP sheet. In addition, the edge of the rivet head compresses on the CFRP workpiece (Fig. 10(*c*)). With the increasing load, stress concentration from the rivet head results in the crack generation which is regarded as a shear failure while the tensile failure mode also occurred in the CFRP sheet which is perpendicular to the loading direction (Fig. 10(*d*)).

It is noteworthy that the proposed model has accurately predicted the joint quality, i.e., low quality and high quality for all the considered cases. Furthermore, scenario D was able to predict the joint quality more accurately as compared to the other scenarios.

## 6 Conclusion

This study develops a predictive model for the online monitoring of the FSBR process in joining CFRP and Al alloy sheets. The

developed method unveils the statistical relationship between the FSBR process and the quality of the joints which is further validated by analyzing joints cross section and failure modes. The key contributions of the present research are as follows.

The proposed data-driven methodology was based on generalizations of the basic PCA-based approach, in extracting features from multi-sensor, high-dimensional, and heterogeneous profile data which were further combined with engineering-driven features (i.e., process parameters, peak force, stacking sequence) to encompass a wholistic process mechanics aspect. The optimal features were then selected from the extracted ones using SGL regression. The selected features were then fed into weighted classifier fusion to evaluate the quality of the FSBR joints through optimizing the classification performance in cross-validation. The available FSBR samples were clustered into a high-quality group and a low-quality group by hierarchical clustering, and their cluster labels were considered as the true quality group labels. The CCRs resulted from various feature extraction methods and feature selection results were assessed and compared. The results indicated that both MPCA and UMPCA were effective feature extraction methods. The average CCR was more than 80%. The proposed method also significantly outperformed the two traditional methods.

The efficacy of the proposed model was validated through experimental results by analyzing the macrostructure and failure modes of the joints. The proposed model emerged as an effective tool for quality prediction as the defective joints (defined through macrostructure) were successfully predicted as the low-quality joints by the model. Furthermore, two additional failure modes, i.e., partial rivet pullout and mixed failure, other than previously observed tensile failure mode were observed. The failure modes were further correlated with macrostructure (mechanical interlocking and ring-shaped residue) where an increase in the thickness of the ring-shaped residue resulted in the transition from high-quality to low-quality joints. The thickness of the residue was found corresponding to the process parameters where high spindle speed and low feed rate yielded thin residue and ultimately high-quality joints. Consequently, the proposed model coupled with experimental results also aids in developing a PSP linkage.

## Acknowledgment

This research is supported by Rutgers Research Council Grant Award and Rutgers University Big Data Pilot Initiative Grant Award. The authors would also like to thank the support from the US National Science Foundation Civil, Mechanical, and Manufacturing Innovation (Grant No. 1664377).

## Conflict of Interest

There are no conflicts of interest.

## Data Availability Statement

The datasets generated and supporting the findings of this article are obtained from the corresponding author upon reasonable request. The authors attest that all data for this study are included in the paper.

## References

[1] Immarigeon, J. P., Holt, R. T., Koul, A. K., Zhao, L., Wallace, W., and Beddoes, J. C., 1995, "Lightweight Materials for Aircraft Applications," Mater. Charact., **35**(1), pp. 41–67.

[2] Che, D., Saxena, I., Han, P., Guo, P., and Ehmann, K. F., 2014, "Machining of Carbon Fiber Reinforced Plastics/Polymers: A Literature Review," ASME J. Manuf. Sci. Eng., **136**(3), p. 034001.

[3] Khan, H. A., Nigar, M., and Chaudhry, I. A., 2015, "Tensile Behavior of Unidirectional Carbon-Reinforced Composites for Aerospace Structures Under Varying Strain Rates," *Applied Mechanics and Materials*, D. Hoxha, I. McAndrew, and A. Dung Ngo, eds., Trans Tech Publications, pp. 357–361.

[4] Wang, K., Li, Y., Banu, M., Li, J., Guo, W., and Khan, H., 2017, "Effect of Interfacial Preheating on Welded Joints During Ultrasonic Composite Welding," J. Mater. Process. Technol., **246**, pp. 116–122.

[5] Upadhyay, P., Hovanski, Y., Jana, S., and Fifield, L. S., 2017, "Joining Dissimilar Materials Using Friction Stir Scribe Technique," ASME J. Manuf. Sci. Eng., **139**(3), p. 034501.

[6] Díaz, J., and Rubio, L., 2003, "Developments to Manufacture Structural Aeronautical Parts in Carbon Fiber Reinforced Thermoplastic Materials," J. Mater. Process. Technol., **143**, pp. 342–346.

[7] Wang, H., Yang, K., and Liu, L., 2018, "The Analysis of Welding and Riveting Hybrid Bonding Joint of Aluminum Alloy and Polyether-Ether-Ketone Composites," J. Manuf. Process., **36**, pp. 301–308.

[8] Khan, H. A., Li, J., and Shao, C., 2017, "Analyses of Friction Stir Riveting Processes: A Review," ASME J. Manuf. Sci. Eng., **139**(9), p. 090801.

[9] Gao, D., Ersoy, U., Stevenson, R., and Wang, P.-C., 2009, "A New One-Sided Joining Process for Aluminum Alloys: Friction Stir Blind Riveting," ASME J. Manuf. Sci. Eng., **131**(6), p. 061002.

[10] Lathabai, S., Tyagi, V., Ritchie, D., Kearney, T., Finnin, B., Christian, S., Sansome, A., and White, G., 2011, "Friction Stir Blind Riveting: A Novel Joining Process for Automotive Light Alloys," SAE Int. J. Mater. Manuf., **4**(1), pp. 589–601.

[11] Wang, W.-M., Ali Khan, H., Li, J., Miller, S. F., and Zachary Trimble, A., 2016, "Classification of Failure Modes in Friction Stir Blind Riveted Lap-Shear Joints With Dissimilar Materials," ASME J. Manuf. Sci. Eng., **139**(2), p. 021005.

[12] Min, J., Li, Y., Li, J., Carlson, B. E., and Lin, J., 2015, "Friction Stir Blind Riveting of Carbon Fiber-Reinforced Polymer Composite and Aluminum Alloy Sheets," Int. J. Adv. Manuf. Technol., **76**(5), pp. 1403–1410.

[13] Khan, H. A., Wang, W. M., Wang, K., Li, S., Miller, S., and Li, J., 2019, "Investigation of Mechanical Behavior of Dissimilar Material FSBR Joints Exposed to a Marine Environment," J. Manuf. Process., **37**, pp. 376–385.

[14] Wang, W., Wang, K., Khan, H. A., Li, J., and Miller, S., 2018, "Numerical Analysis of Magnesium to Aluminum Joints in Friction Stir Blind Riveting," Procedia CIRP, **76**, pp. 94–99.

[15] Guo, W., Chen, J., Guo, S., and Li, J., 2017, "Process Monitoring of Friction Stir Blind Riveting for Lightweight Materials," Proceedings of the 2017 Industrial and Systems Engineering Conference, Pittsburgh, PA, pp. 2165–2170.

[16] Lu, H., Plataniotis, K. N., and Venetsanopoulos, A. N., 2008, "MPCA: Multilinear Principal Component Analysis of Tensor Objects," IEEE Trans. Neural Netw., **19**(1), pp. 18–39.

[17] Lu, H., Plataniotis, K. N., and Venetsanopoulos, A. N., 2009, "Uncorrelated Multilinear Principal Component Analysis for Unsupervised Multilinear Subspace Learning," IEEE Trans. Neural Netw., **20**(11), pp. 1820–1836.

[18] Min, J., Li, J., Carlson, B. E., Li, Y., Quinn, J. F., Lin, J., and Wang, W., 2015, "Friction Stir Blind Riveting for Joining Dissimilar Cast Mg AM60 and Al Alloy Sheets," ASME J. Manuf. Sci. Eng., **137**(5), p. 051022.

[19] Paynabar, K., Jin, J. J., and Pacella, M., 2013, "Monitoring and Diagnosis of Multichannel Nonlinear Profile Variations Using Uncorrelated Multilinear Principal Component Analysis," IIE Trans., **45**(11), pp. 1235–1247.

[20] Guo, W., Jin, J., and Hu, S. J., 2016, "Profile Monitoring and Fault Diagnosis Via Sensor Fusion for Ultrasonic Welding," Proceedings of the ASME 2016 11th International Manufacturing Science and Engineering Conference. Volume 2: Materials; Biomanufacturing; Properties, Applications and Systems; Sustainable Manufacturing, Blacksburg, VA, p. V002T04A028.

[21] Yan, H., Paynabar, K., and Shi, J., 2015, "Image-Based Process Monitoring Using Low-Rank Tensor Decomposition," IEEE Trans. Autom. Sci. Eng., **12**(1), pp. 216–227.

[22] Cichocki, A., Mandic, D., De Lathauwer, L., Zhou, G., Zhao, Q., Caiafa, C., and Phan, H. A., 2015, "Tensor Decompositions for Signal Processing Applications: From Two-Way to Multiway Component Analysis," IEEE Signal Process. Mag., **32**(2), pp. 145–163.

[23] Bilodeau, M., and Brenner, D., 2008, *Theory of Multivariate Statistics*, Springer Science & Business Media, New York.

[24] Friedman, J., Hastie, T., and Tibshirani, R., 2001, *The Elements of Statistical Learning*, Springer Series in Statistics, New York.

[25] Grasso, M., Colosimo, B., and Pacella, M., 2014, "Profile Monitoring Via Sensor Fusion: The Use of PCA Methods for Multi-Channel Data," Int. J. Prod. Res., **52**(20), pp. 6110–6135.

[26] Friedman, J., Hastie, T., and Tibshirani, R., 2010, "A Note on the Group Lasso and a Sparse Group Lasso," preprint arXiv:1001.0736.

[27] Simon, N., Friedman, J., Hastie, T., and Tibshirani, R., 2013, "A Sparse-Group Lasso," J. Comput. Graph. Stat., **22**(2), pp. 231–245.

[28] Yuan, M., and Lin, Y., 2006, "Model Selection and Estimation in Regression With Grouped Variables," J. R. Stat. Soc. B: Stat. Methodol., **68**(1), pp. 49–67.

[29] Ruta, D., and Gabrys, B., 2000, "An Overview of Classifier Fusion Methods," Comput. Inf. Syst., **7**(1), pp. 1–10.

[30] Schön, J., 2004, "Coefficient of Friction for Aluminum in Contact With a Carbon Fiber Epoxy Composite," Tribol. Int., **37**(5), pp. 395–404.

[31] Khan, H. A., Pei, S., Chen, N., Miller, S., and Li, J., 2020, "Evaluation of μFSBR Joint Performance by Process-Physics Based Quality Criteria and Online Monitoring Algorithm," J. Mater. Process. Technol., **278**, p. 116508.

[32] Min, J., Li, Y., Li, J., Carlson, B. E., and Lin, J., 2015, "Mechanics in Frictional Penetration With a Blind Rivet," J. Mater. Process. Technol., **222**, pp. 268–279.